

Allosteric Modulation of Human Dopamine Transporter Activity under Conditions Promoting its Dimerization

Mary Hongying Cheng,¹⁺ Jennie Garcia-Olivares,²⁺ Steven Wasserman², Jennifer DiPietro², and Ivet Bahar^{1*}

From ¹the Department of Computational and Systems Biology, School of Medicine, University of Pittsburgh, Pittsburgh, PA 15260; and ²Laboratory of Molecular and Cellular Neurobiology, National Institute of Mental Health, NIH, Bethesda, MD 20892.

Running title: *Human dopamine transporter dimerization*

*To whom correspondence should be addressed: Ivet Bahar, Department of Computational and Systems Biology, School of Medicine, University of Pittsburgh, 3064 BST 3, 3501 Fifth Avenue, Pittsburgh, PA 15213. Phone: 412 648 3332; Fax: 412 648 3163; e-mail: bahar@pitt.edu

Keywords: Neurotransmission, dimerization, dopamine transporter, structure and dynamics, mechanism of function, cooperative transition

ABSTRACT

The human dopamine (DA) transporter (hDAT) is a key regulator of neurotransmission and a target for antidepressants and addictive drugs. Despite the recent resolution of dDAT structures from *Drosophila melanogaster*, complete understanding of its mechanism of function and even information on its biological assembly is lacking. The resolved dDAT structures are monomeric, but growing evidence suggests that hDAT might function as a multimer, and its oligomerization may be relevant to addictive drug effects. Here, using structure-based computations, we examined the possible mechanisms of hDAT dimerization and its dynamics in a lipid bilayer. Using a combination of site-directed mutagenesis, DA-uptake, and cross-linking experiments that exploited the capacity of Cys306 to form inter-monomeric disulfide bridges in the presence of an oxidizing agent, we tested the effects of mutations at transmembrane segment (TM) 6 and 12 helices in HEK293 cells. The most probable structural model for hDAT dimer suggested by computations and experiments differed from the dimeric structure resolved for the bacterial homolog, LeuT, presumably because of a kink at TM12 preventing favorable monomer packing. Instead, TM2, TM6, and TM11 line the dimer interface. Molecular dynamics simulations of the dimeric hDAT indicated that the two subunits tend to undergo cooperative structural changes, both on local (extracellular gate opening/closure) and global

(transition between outward-facing and inward-facing states) scales. These observations suggest that hDAT transport properties may be allosterically modulated under conditions promoting dimerization. Our study provides critical insights into approaches for examining the oligomerization of neurotransmitter transporters to shed light on their drug modulation.

Dopamine (DA) transporter (DAT) regulates dopaminergic signaling by reuptake of DA into presynaptic terminals, thus preventing excess DA levels at the synapse. The process is assisted by co-transport of two sodium ions and the permeation of a chloride ion. The human DAT, hDAT, is a major target for therapeutic antidepressants and addictive drugs such as amphetamine (AMPH) and cocaine (1-3). Dysfunction of hDAT has been implicated in many neurological and psychiatric disorders (2,3).

DAT belongs to the SLC6A3 family of neurotransmitter sodium symporters (NSS). NSSs comprise structural and functional homologs such as norepinephrine transporter (NET), serotonin transporter (SERT) and GABA transporter (GAT). It is generally accepted that NSS members transport their substrate via the classic alternating access mechanism (4), i.e. the transporter alternates between outward-facing open (OF_o) conformation for extracellular (EC) binding of DA and Na⁺/Cl⁻ ions, and inward-facing open (IF_o) conformation for their intracellular (IC) release. The passage between these states takes place via intermediates occluded to both EC and IC

regions, either in substrate/ Na^+ -loaded form, or in *apo* state following the release of the cargo. In addition, eukaryotic NSS members such as DAT and SERT allow for the efflux of their substrate to the cell exterior, which has been attributed to the modulating effects of addictive psychostimulants such as AMPH (5,6).

NSS members generally share the topology of the bacterial leucine transporter LeuT. The LeuT fold is composed of twelve transmembrane (TM) helices (TM1–TM12) organized in two pseudo-symmetric inverted repeats (7). LeuT has long served as a prototype for understanding the mechanism of function of transporters that share its fold, as the first structurally characterized member of the LeuT fold family. The Gouaux laboratory has resolved the X-ray structures of LeuT in four different states: OFo, stabilized by inhibitors (8), substrate-free OFo (9), substrate-bound OFc where the EC gate is closed (10), and *apo* IFo (9). Molecular modeling and simulations based on known LeuT structures have helped draw useful inferences on the structure and dynamics of hDAT (11-15). On a broader scale, computational studies performed for transporters that share the LeuT fold provided insights into the mechanistic aspects of substrate transport favored by NSSs (16-23).

The elucidation of the first DAT structure (antidepressant-bound dDAT, from *Drosophila melanogaster*) in OFo state (24), and subsequent resolution of DA-, AMPH- or cocaine-bound dDAT (25), have led the way to structure-based explorations of DAT mechanism of function (26-28). dDAT has more than 50% sequence identity with hDAT, as opposed to 22% with LeuT. As such it served as a reliable model for modeling its human counterpart. Using these structural data, we studied the mechanism of function of hDAT monomer (27), with dual-boost accelerated MD (aMD) (29,30) and conventional MD (cMD) simulations. Our simulations revealed the structure of hDAT at various stages of the transport cycle, including DA-bound OFc state that shows close resemblance to Leu-bound LeuT (10), and the IFo state leading to the release of DA and Na^+ ions. The transport events revealed for hDAT monomer (27) showed striking similarities to those disclosed in our recent investigation of LeuT transport cycle (16,17). Yet, there are notable differences in the sequence and structure of DAT and LeuT, which evidently underlie their specific functionalities.

A prominent structural difference is the kink in the TM12 helix of dDAT (24) which is also retained in hDAT (Fig. 1). This kink occurs at the position of two serines (Ser567-Ser568 in hDAT) that are conserved among human monoamine transporters hDAT, hSERT and hNET as well as inhibitory transporters like hGAT1 and glycine transporters (hGly1). The recently resolved crystal structure of hSERT in an antidepressant-bound OFo also shows a kink at TM12 (31).

At present, there is no consensus on whether the preferred functional state of NSS members is monomeric or dimeric, or even oligomeric. LeuT OFo and OFc crystal structures were resolved as dimers (8-10). Moreover, the Gouaux lab studied LeuT crystal structures in a range of environments and reported that a common feature was the occurrence of a parallel LeuT dimer (32). Even though dDAT (24,25) and hSERT (31) have been resolved as monomeric constructs, there is growing evidence in support of the formation of multimeric structures for monoamine transporters such as hDAT or SERT, indicated by radiation inactivation (33), crosslinking (34), mutagenesis (35), co-immunoprecipitation (36,37), and single molecule analysis (38).

Using fluorescence resonance energy transfer microscopy, Sitte and coauthors provided the first visual evidence in support of the oligomerization of SERT and GAT1 in living cells (39). The same group subsequently showed the importance of a leucine heptad repeat in GAT1 oligomerization (40). They have also shown that GAT1 functional subunit is the monomer. Oligomerization of NSSs has been suggested to be a determinant of transporter trafficking to the plasma membrane in addition to efficient substrate transport (37,40,41). A cooperativity has been observed recently within DAT oligomers (42); and NSS oligomeric constructs have been proposed to be implicated in AMPH action via an oligomer-based counter-transport model (43), as reviewed by Sitte and coworkers (5,44). An early experimental study by Javitch and coworkers found that the dimer interface of hDAT formed intermonomeric cross-links between the C306 residues belonging to the TM6 of the two subunits (34). Torres and coworker proposed that the TM2 segment of hDAT was involved in dimerization (35). On the other hand, the dimer interface observed in prokaryotic LeuT is mainly formed by TM9 and TM12 (8,10).

No rigorous computational study of potential dimerization interface has been performed after the elucidation of the monomeric DAT structure. Given the neurobiological significance of the transporter and the availability of structures, we are now in a good position to examine the possible dimerization geometry and/or the most favorable dimerization interface, as well as their implication on DAT functional dynamics using a combination of computations and experiments. To this aim, we take advantage of the wealth of conformational data generated in our hDAT monomer simulations (26,27): mainly, we will explore the dimerization propensities of hDAT in different states in the presence of the membrane remodeling effect.

Strikingly, the most probable hDAT dimer model indicated by the present study differs from the LeuT dimeric structure with regard to its dimerization interface. C306 residues are confirmed to form inter-monomer crosslinks in

the presence of the oxidizing agent copper-phenantroline (CuP), in support of the computationally predicted dimerization interface, and in consistency with the observations made by Javitch and coworkers (34). Our results indicated that residues in (spatial) proximity of C306 are important for hDAT stabilization and dimer formation. R304 and E307 appear to be able to form inter-subunit salt-bridges in our computed model. Substitutions at those sites (changes to alanine, R304A and E307A; or charge inversions, R304E and E307R) resulted in impairment of the formation of the CuP-induced dimer. Moreover, our study highlights the functional significance of the kink in the TM12 segment of hDAT. Substitution of helix-breaking residues (G561, S567, S568 and P573) at this kink by their (helix-favoring) orthologous counterparts in LeuT reduced the surface expression of DAT and altered its DA-reuptake. The importance of the TM12 residues revealed a new region relevant to function and/or expression.

Results

Validation of the computed LeuT dimer structure with that structurally resolved—To assess the accuracy of ClusPro (45) for predicting the dimeric structure of a member of LeuT fold family, we first examined LeuT in different conformation states. LeuT dimer in the OFo state has been resolved by X-ray crystallography (9). We took one monomer (subunit A) from the OFo LeuT dimer crystal structure (PDB: 3TT1) and then generated structural models for a dimer composed of these monomers using ClusPro. Among the 23 computationally predicted models for LeuT dimer, only one satisfied the four criteria of acceptance (see Experimental Procedures). **Fig. S1A** compares this computationally predicted LeuT OFo dimer with that structurally resolved. The root-mean-square deviations (RMSD) between the computed structural model (*yellow*) and experimentally resolved structure (*orange*) is 1.39 Å, indicating that the model predicted for the LeuT dimer in OFo state yields satisfactory agreement with the structure determined by X-ray crystallography.

The LeuT dimer in the IFo state has not yet been resolved. We generated a structural model for the IFo LeuT dimer using ClusPro, based on the resolved IFo LeuT monomer (PDB: 3TT3), using precisely the same protocol as adopted for OFo dimer (which will also be adopted for hDAT below). Interestingly, among a total of 27 LeuT IFo dimer models, again only one satisfied the four criteria set forth for selecting the optimal model. **Fig. S1B** displays the structural alignment of the computationally predicted LeuT dimers in the OFo (*yellow*) and IFo (*green*) states. The RMSD between these two structural models is ~6Å. Similar protein orientation and interfacial contacts were preserved

in different states. The interface predominantly involves contacts between the pair of TM12 helices belonging to the two subunits, consistent with experimental data (**Fig. 2A**).

Taken together, ClusPro dimer docking tool is verified here to closely reproduce the dimerization geometry of the OFo monomers with an RMSD: 1.39Å with respect to the crystal structure (9). It also helps us build a structural model for the dimer formed by two monomers in the IFo state, which satisfies the constraints inferred from previous experiments, yet to be experimentally resolved. We now proceed to the evaluation of dimerization geometry for hDAT.

Discrepancy between experimental LeuT dimer contact and computational prediction for hDAT dimer—The LeuT dimers resolved in the OFo (9) and OFc states (10) make interfacial contacts between their transmembrane helices TM12, complemented by TM9, and a small segment from the EL2 loop (I161 to K163) (see **Fig. 2A**). In contrast, the same methodology applied to hDAT ended up yielding a significantly different dimerization interface (**Fig. 2B**). The best structural model computed hDAT dimer showed an association between TM2, TM6 and TM11 portions. Specifically, the predicted hDAT dimer interface includes V100-P112 in TM2, part of TM6a (F302-W311), and S517-F543 in TM11 (see **Fig 2B**). Javitch group showed that the hDAT dimer was associated by potential cross-linking of C306 at the TM6 segment (34). In the hDAT OFo and IFo dimer models predicted by ClusPro, the distance between the C306 residues from the two subunits is within 10.0±3.5 Å. The distance is close enough to allow for the formation of cross-links in the presence of oxidizing agents, facilitated by fluctuations in inter-residue distances.

In our hDAT dimer models, there is a large hydrophobic patch at the interface (Supplementary figure **Fig. S2A**). Experimental work by Torres et al suggested that a leucine zipper (L99, M106, L113 and L120) in TM2 of hDAT might contribute to the dimerization of hDAT (35). In our computed dimer model, the suggested leucine zipper was not in direct contact (**Fig. S2B**). Instead, residues V100, V107 and P112 contributed to hydrophobic interfacial interactions. This shift by one residue notwithstanding, both computational modeling and experimental study suggest that the TM2 segment may contribute to stabilize the dimer interface (see **Fig 2B**).

Significance of the kink in the TM12 segment of DAT—In summary, on the one hand, the structural model predicted hDAT dimer showed good accord with cross-linking (34) and mutagenesis studies on hDAT (35). On the other, the predicted intersubunit interface in hDAT differed from that seen in the prokaryotic LeuT dimer crystal structures (see **Fig 2**). This difference could be attributed to the sharp kink

in the TM12 segment (Fig. 1), which prevents the registration of the two TM12 helices at the interface. Notably, the same kink has been observed in the crystal structures of dDAT (24,25) and hSERT (31). Furthermore, the eukaryotic NSSs and bacterial LeuT show significant structural difference at the C-terminal segment (Fig. 1). Eukaryotic transporters have a large C-terminal domain, which may further hinder the efficient packing of these regions against each other in the dimeric state.

To investigate how the kink in TM12 affects hDAT function, we generated a series of DAT mutants expressed them into HEK293 cells, and measured their cell surface expression and DA-uptake capacity. Substitution of the kink forming residues G561, S567, and S568 by their orthologous counterparts in LeuT (i.e. G561A, S567F and S568L), and the helix-breaking P573 by alanine (P573A) resulted in a significant reduction in surface expression levels of the mutants compared to the wild type (WT) transporter (Fig. 1E). Because the protein expression for all mutants was different, we normalized the specific [³H]-DA uptake properties of the mutants with respect to their surface expression, so as to allow for the comparison of the DA transport activities of the mutants to that of WT-hDAT (Table 1). Fig. 1F shows that the transport activities of G561A and P573A were significantly reduced. In contrast, the mutants S567F and S568L, which displayed similar levels of expression, showed an increased DA transport activity compared to WT-hDAT (Fig. 1F).

Structural transitions of protomers in hDAT dimer resemble those observed in the monomer alone

To further investigate the structural stability and dynamics of the computationally-predicted hDAT dimer in the OFo and IFo state, we performed four 100-ns MD simulations of hDAT dimers embedded in solvated POPC lipids. A typical MD simulation system constructed for simulating the dynamics of hDAT dimer is shown in Fig. 3A. In all four runs (two performed for each dimeric structure), the RMSD of the dimer reached an asymptotic value of 3.0 ± 0.4 Å after 10 ns simulations, and fluctuated near this value in the remaining 90 ns, in support of the stability of the structural models embedded in the lipid bilayer. Fig. 3B illustrates the alignment of 100-ns MD equilibrated hDAT dimer in the OFo and IFo states. The corresponding RMSD is ~ 3.5 Å. Notably, the two dimers show different tiltings at the EC-exposed and IC-exposed TM helices, e.g. TM1a (IC-exposed half of the broken helix TM1) is wide open in the IF state; whereas the helices near the EC vestibule are relatively more closed than their OF counterparts. Overall, the opening/closure of the EC and IC vestibule in the dimer (Fig. 3C) closely resembles those previously observed in the monomer dynamics (27).

For a quantitative analysis of the structural characteristics of the OF and IF dimers, we further examined the time evolution of the relative positions of selected pairs of helices which provide a metric for probing the degree of exposure of the EC and IC vestibules. In line with previous work (26,27), two pairs of helical segments were used as probes: TM1b and TM10 for exposure to the EC medium, and TM1a and TM6b for exposure to the IC medium. We performed four runs of 100 ns each (duplicate for each dimer, designated OF_1, OF_2, IF_1 and IF_2). Fig. 4 shows that the time evolution of the distance between these pairs of helices in the OF (panels A and B) and IF (panels C and D) dimers.

The OF dimer in run OF_1 underwent a local structural transition from conformation OFo to OFc as can be seen from the time evolution of the TM1b-TM10 distance (*light* and *dark blue* curves, for respective subunits A and B) in Fig. 4A. Closer examination showed that the EC gates F320-Y156 and R85-D406 closed almost simultaneously within 20 ns in both subunits, leading to the OFc state (Fig. 5). Notably, the closure of EC gates was similarly observed in simulations of hDAT monomer (26,27). In run OF_2, the subunits remained open (Fig. 4B); the TM1b-TM10 distance of 20 Å, typical of OFo conformer, was maintained during the course of simulations, with fluctuations within the range ascribed (26,27) to the OFo state. In both runs OF_1 and 2, the IC-exposed helical pairs TM1a and TM6b (*dark/light red*) remained tightly packed (Fig. 4A-B), again consistent with the closed conformation of the IC gate in the OF state of the transporters.

The relative distances of the two pairs of helices were inverted in the IF dimers (Fig. 4C-D), consistent with the opening of the IC gate and closure of the EC gate in the IF state. In the run IF_1, the IC vestibule of subunit A remained open while that of subunit B gradually closed, as can be seen from the time evolution of TM1a-TM6b helices. In run IF_2 (Fig. 4D), both helix pairs showed the same behavior, i.e. a transition toward the IFc state. In 3 out of 4 cases, the subunits in IFo dimer exhibited a natural tendency to rearrange themselves in favor of a potential transition into the OF state – a transition that is functionally required for completing the transport cycle.

Overall these data demonstrate that the OF and IF dimeric forms have distinctive interhelical packing characteristics (compare panels A-B for OF dimers to panels C-D for IF dimers), while the two subunits within the individual dimers exhibit similar dynamic patterns (compare the *dark* and *light* colored curves in each case). The equilibrium values observed for those interhelical distances and their fluctuation ranges were again typical of those sampled by the OF or IF monomers in isolation. Interestingly, the two subunits in a given dimer exhibited a tendency to undergo similar conformational transitions in

most runs, i.e., both remained in OF_o state; or both transitioned to OF_c state in the respective runs OF_2 and OF_1; and both subunits exhibited a tendency to progress toward OF state in IF_2 (Fig. 4).

Oxidative cross-linking experiments show that TM6 residues are important for hDAT stabilization and dimer formation-

In the initial generation of the dimeric structure and the construction of the MD environment, we did not impose disulfide bond formation between C306 residues from the neighboring subunits. During MD simulations, the average distance between the two C306 decreased to $7.5 \pm 2.5 \text{ \AA}$ and $8.0 \pm 1.5 \text{ \AA}$ in the respective OF and IF dimers, in favor of a possible disulfide bridge formation. In addition to C306, C523 residues from the interfacial TM11 segments (Fig. 6A) came into proximity ($11.0 \pm 1.5 \text{ \AA}$). While a Cys at position 306 is unique to hDAT, C523 is fully conserved among the eukaryotic NSSs and could not be (solely) responsible for the distinct dimerization behavior of LeuT and hDAT (Fig. 2). We also noted in the computed model a number of charged amino acids that are likely to make interfacial contacts, and even form salt bridges in the IF conformation of the dimer, e.g., E307(A)-R304(B) and/or E307(B)-R304(A) (Fig. 6B). Acidic and basic residues at the respective sequence positions 307 and 304 are highly conserved in the eukaryotic NSSs (Fig. 6C). We hypothesized that mutations at these residues might affect the intersubunit disulfide crosslinking at C306 and/or overall hDAT function. We introduced alanine substitutions at R304 and E307 and at the two native cysteines C306 and C523. Like the mutations in TM12, the levels of expression were different for all mutants (Table 1); so we normalized the [³H]-DA-uptake with respect to surface expression so as to enable a comparative analysis across the mutants, and with WT-hDAT. C306A mutant showed DA-uptake capacity comparable to that of WT hDAT (Table 1). Unexpectedly the mutants C523A, R304A and E307A displayed increased transport activity compared to WT hDAT.

To explore whether these residues participate in the stabilization of the hDAT dimer, we examined the propensity of C306 in hDAT to dimerize with the neighboring subunit in the presence of CuP in intact HEK293 cells. In WT hDAT-expressing cells, CuP treatment resulted in the appearance of a distinct band at 150 kDa in addition to immunoreactive bands at 50, 75 and 100 kDa (Figs. 7A-B and E), which represent the immature and mature hDAT monomeric forms (50 and 75kDa) and the immature dimer (app. 100 kDa) (34,46,47). It has been shown previously that the alanine substitution C306A completely abolishes the formation of DAT dimers by CuP (34). As expected, C306A did not produce a crosslinked species after CuP treatment (Figs. 7A-B and E), confirming

that C306 is the reactive residue at the CuP-induced dimer interface. CuP treatment of cells expressing C523A, R304A and E307A resulted in the formation of the 150 kDa-DAT adduct corresponding to CuP-induced dimer (Fig. 7A-B).

We also generated two additional hDAT mutants, R304E and E307R, to evaluate the effect of the proposed salt-bridges on hDAT function and oligomerization. The E307R substitution increased transport activity (Table 1) and retained modest ability to form the CuP-induced dimers (Fig. 7C-D). The most dramatic effect on dimer formation was observed with the R304E mutation. In cells expressing R304E, treatment with CuP resulted in no formation of the 150 kDa DAT adduct (Fig. 7D-E). Finally, we estimated the relative amount of CuP-induced dimer in comparison with the amount of dimer present in the control group (no CuP) for each mutant (Fig. 7F). In this analysis we observed that WT and C523A hDAT produced comparable amounts of CuP-induced DAT dimer. Moreover, other mutations in R304 (R304A) and E307 (E307A and E307R) resulted in a reduction of CuP-induced dimer compared to the dimer formed in the WT, and the mutation R304E completely abolished the formation of 150 kDa DAT adduct, in support of the idea that these nearby residues are important for maintaining the protein in a conformation that permits crosslinking and likely favors dimerization.

Discussion

In the present study, we constructed hDAT dimers composed of subunits in the OF and IF states using structural data for monomers generated in our recent MD simulations of hDAT (27). While the LeuT dimer displays interfacial contacts at the TM9 and TM12 segments (Fig. 2A) (indicated by experiments and reproduced by the presently adopted computational protocol), subunits in the computed hDAT dimer are preferentially associated through portions of their TM2, TM6 and TM11 helices (Fig. 2B). Among these three helices, TM6 participates in the substrate/Na⁺/Cl⁻ binding pocket, and TM2 participates in chloride binding. Closer examination showed that the TM6 portions that make interfacial contacts (near C306, EC exposed end) differ from those involved in coordinating the substrate and ions (almost halfway into the lipid bilayer), such that the substrate/Na⁺/Cl⁻ binding site is not affected by dimerization. Likewise, comparison of isolated monomer chloride binding site and that in the monomer belonging to the dimer shows that the chloride coordination geometry is maintained in the dimer. There is a conserved tyrosine (Y102 in hDAT) that interacts with the chloride ion, whose site chain reorientation (away from the interface) remains unchanged. Overall, the dimerization interface does not have any direct effect on the local interactions in the substrate/Na⁺/Cl⁻ binding site; and the mechanism of opening/closure of the EC and IC vestibules in the dimeric

form of DAT (**Fig. 3C**) closely resembles that observed (27) in its monomeric form.

A central kink was observed to prevent the parallel alignment of the pair of TM12 helices in hDAT (**Figs. 1B-C**). This irregularity of TM12 at a sequence region comprised of two consecutive serines is not unique to hDAT. On the contrary, this is a common feature among eukaryotic neurotransmitter transporters that share the LeuT fold, which distinguish them from the bacterial transporter LeuT (**Fig. 1D**). While current experiments do not provide direct evidence on the position of TM12 with respect to the dimer interface, they reveal the functional significance of a series of residues at the TM12 kink site. Substitutions by their LeuT counterparts (G561A, S567F, S568L or P573A) led to a decrease in surface expression levels (~70% to ~90% reduction). Their low levels of expression prevented us from pursuing the oxidative crosslinking experiments. We normalized the observed DA-uptakes by the levels of surface expression to analyze the intrinsic uptake capacity of each mutant. In this analysis, we observed that two TM12 mutations, G561A and P573A resulted in a significant loss of uptake activity (~80% and ~30%, respectively) (**Figs. 1E-F; Table 1**). In contrast, the two others (S567F and S568L) showed an increase (~200% and ~50%, respectively) in the apparent uptake capacity when compared with WT DAT. These results revealed that these residues might play a role in protein maturation, folding or structural dynamics, and thereby on transport activity. The observed differences between their effects reflect that each mutation confers specific changes to the carrier. We conclude that G561A and P573A result in non-functional carriers while S567F and S568L cause an impairment in DAT trafficking. Yet, the small number of S567F and S568L mutants that actually reach the cell surface are fully functional. Additionally, the computational analysis shows that S568 forms a hydrogen bond with S483 from TM10 helix (**Fig. 1C**). TM10 has been shown in our recent study to undergo a significant reconfiguration during the transport (27). It remains to be tested, for example with the help of the mutant S483G (LeuT counterpart), if such hydrogen bond formation contributes to gain of transport activity. It is striking to see that these TM12 residues that partly form the scaffolding domain of hDAT and are not in direct contact with the DA-translocation pathway, resulted in non-functional carriers in G561A and P573A.

The present study shows that in the presence of an oxidizing agent that promotes disulfide-bridge formation, hDAT exhibits a tendency to increase dimerization, due to cross-linking of C306(A)-C306(B) (**Fig. 7**). This observation lends strong support to the dimerization interface different from that of LeuT, predicted by our computational model for hDAT dimer. Other residues proposed here to play key roles are the charged residues

(E307 and R304) (**Figs. 6-7**), that potentially form an interfacial salt bridge.

For each state, we performed two sets of 100 ns MD simulations of hDAT dimer embedded into solvated membrane (**Fig. 3A**) to examine the stability of the structural models and the local changes in structure that may be functionally relevant. In all runs, the RMSDs were stabilized at 3.0 ± 0.5 Å with respect to the initial models within the first 10 ns, and remained unchanged in the remaining 90 ns portion of the trajectories. RMSD between MD-equilibrated hDAT OFo and IFo dimers (**Fig. 3B**) was around 3.5 ± 0.8 Å. The hDAT OFo and IFo dimer exhibited distinctive characteristics in their EC-exposed and IC-exposed inter-helical distances, with values similar to those observed in the respective monomeric OFo and IFo states (27). Notably, the closure of EC gates (R85-D476 and Y156-F320) upon binding of Na^+ , Cl^- and DA was clearly seen in the dimer (**Figs. 4 and 5**), similar to that observed in the hDAT monomer (26,27).

Interestingly, the two subunits in a given dimer generally exhibited coupled transitions during MD runs (**Figs. 4 and 5**). While it is hard to generalize based on four runs, the fact that a coupled behavior was observed between subunits in several independent runs suggests that there may be a correlation between the dynamics of the two subunits. The majority of earlier experimental studies did not directly indicate a cooperativity among protomers. Kilic and Rudnick provided the first experimental evidence showing a dimeric form of SERT with functional interactions between subunits (36). Furthermore, cooperativity between the NSS monomers has been observed in recent experiments on DAT (42). Our recent computational study (48) using the anisotropic network model (49) suggests that dimerization of LeuT or hDAT alters the collective motions intrinsically accessible to the individual monomers in favor of the functional transitions (OF \leftrightarrow IF). Whether the subunits in the dimer tend to undergo coupled changes is worth further investigating. It is not clear whether this coupling is due to the adoption of the same conformational state for both subunits as initial configuration; the initial conformers relaxed within the first 20 nanoseconds. Mixed conformations (containing one subunit in IF state and two others in OF or one in an intermediate OF) have been observed for another family of transporters (50,51), and it remains to be seen if the LeuT fold also favors such mixed conformations. In the future it might be of interest to explore the possibility of mixed (IF and OF) dimeric structures and examine their relative stability (or interfacial surface area) and dynamics. The present study does not preclude the possible occurrence of higher oligomerization states, or a distribution of multimers in different oligomerization states. Likewise, there may be alternative dimerization states with different probabilities. Other neurotransmitter transporters

have been observed for form dimers or trimers, while maintaining the monomeric fold; and oligomerization properties of hDAT and their functional implications may need further analyses. Finally, while a symmetric arrangement was used as a criterion for generating possible dimerization geometries, the final models exhibited only pseudosymmetric arrangements.

The function of NSSs is mediated by regulatory proteins (i.e. CaMKII), additive drugs (i.e. AMPH), and anionic lipids PIP₂ (see (3,5)). Interestingly, anionic lipids palmitoyl-oleoyl phosphatidyl glycerol (PG) were found to bind at the interface of trimeric NSS ortholog betaine transporter BetP (52). We hypothesize that anionic lipids (i.e. PIP₂) may potentially bind at the interface of hDAT dimer, as resolved in its NSS ortholog BetP (52), or reported to mediate stable oligomer constructs in hSERT (53); in addition, regulatory proteins or additive drugs, may bind at the interface of hDAT dimer or higher order constructs for cooperative modulation. Our study provides insights into methods for exploring the oligomerization of NSSs and shedding light on the functional cooperativity and drug modulation of NSSs. In the future, it would be of interest to explore the potential binding of regulatory proteins or anionic lipids PIP₂ to NSS oligomer and understand the cooperativity between the NSS monomers using combined experimental and computational studies.

Experimental Procedures

Computational

Construction of hDAT dimer – We have generated *in silico* hDAT monomer conformations at different stages of the transport cycle (27). We focused on the conformers in the OFo and IFo states to construct structural models for hDAT dimer. For each state, three representative conformers were selected, which were used for generating dimers using the *dimer docking* module in ClusPro (<https://cluspro.bu.edu>) (45). For the OFo state, we chose the conformers stabilized after 2-10 ns MD equilibration in the presence of DA, two Na⁺ and a Cl⁻, before proceeding to the OFc state; and for the IFo state, hDAT IF conformers sampled after releasing DA and ions to the IC region were selected, which were further subjected to 2 μ s MD simulation using the Anton special-purpose computer (54).

For each simulation performed with a different monomer conformer, up to 30 dimeric models were predicted by ClusPro. These were rank-ordered based on the docking score from ClusPro, together with four criteria specific to NSS membrane proteins: (1) symmetric or pseudo-symmetric arrangement of the monomers; (2) exposure of the N- and C- termini to the IC region; (3) proper orientation of the aromatic residues (i.e., Trp) on the EC and IC sides to enable suitable anchoring the

protein to the membrane; and (4) maintenance of similar interfacial contacts between the dimer formed by the OF monomers and that formed by IF monomers. Although up to 90 structural models (three runs with ~30 models) were generated for each state, these requirements were met by 5-6 models for each state. The RMSD between any pair of dimeric conformers selected by this screening procedure was observed smaller than 2.0 Å for OFo dimers, and 4.5 Å for IFo dimers. A representative conformer (which has the lowest RMSD with respect to all others in each ensemble) was selected for each (OFo and IFo) state. More details on the methodology are presented in a recent study (48).

For testing our protocol, we reconstructed *in silico* the LeuT dimer in the OFo state (Fig. 2A) using the structural data on one monomer (subunit A) from the dimeric structure resolved for LeuT (PDB: 3TT1) (8,10). The structural model computationally-predicted to be the most favorable dimerization state was verified to closely agree with that resolved by X-ray, lending support to the applicability of our protocol for constructing dimeric models.

Construction of MD simulation environment for hDAT dimers

– The systems were set up using VMD (55). For the OFo hDAT dimer, a DA, two Na⁺ ions and one chloride ion were bound using coordinates from previous work (27). No substrate/ions were included in the IFo dimer. The TM portion of the hDAT dimer was then inserted into the center of a pre-equilibrated 1-palmitoyl-2-oleoyl-sn-glycero-3-phosphocholine (POPC) bilayer, following previous protocol (27). Fully equilibrated TIP3 waters were added to form a rectangular simulation box of 140 Å×140 Å×100 Å³. Na⁺ and Cl⁻ ions were further added to obtain a 0.15M neutral solution. Overall, each simulation system contained approximately 1.8 x 10⁵ atoms, including the hDAT dimer, 400 lipids, and 35,000 water molecules.

MD simulations and trajectory analysis – All simulations were performed using NAMD2 (56). Simulation parameters and methods were adopted from our simulations of hDAT monomer (27). Briefly, we used the CHARMM force field with CMAP corrections (57,58) for hDAT, water and lipid molecules; the parameters for the substrate DA were evaluated following the protocol in CHARMM General Force Field (CGenFF) for drug-like molecules (59). Prior to productive runs, each system was first energy-minimized for 50,000 steps, followed by 0.5 ns constant volume and temperature (310K) (NVT) simulations and a subsequent 4 ns Nosé-Hoover constant pressure (1bar) and temperature (310 K) (NPT) simulation, during which the protein was fixed and constraints on the POPC head groups were gradually released. Subsequently, the constraints on the protein backbone were reduced from 10 kcal/mol to zero

within 3 ns. Finally, the unconstrained protein was subjected to NPT simulations.

For each dimer, two independent MD runs of 100 ns were performed, designated as OF-1 and OF-2, and IF-1 and IF-2. VMD (55) with in-house scripts was used for visualization and analysis of MD trajectories. For calculating the RMSD, hDAT residues R58-E598 from both subunits were used, except for the structurally unresolved EL2 loop segment (S190-P212). The opening of the EC gates was assessed by the changes in center of mass (CoM) distances between the residues Y156 and F320 that serve as the inner gate, and R85 and D476 that serve as the outer gate. Calculations of inter-helical distances were based on residues K66-V78 (TM1a), L80-Q93 (TM1b), A308-L322 (TM6a), F326-Y335 (TM6b), and G467-G481 (EC-exposed TM10 segment).

Experimental

cDNA constructs, Mutagenesis and heterologous expression- Single point mutations were introduced into a cDNA construct of hDAT inserted in the vector pcDNA3.1(+) (Invitrogen) using the site-directed mutagenesis kit Q5® (New England Biolabs). To generate primers the NEBaseChanger web-based tool was used (www.neb.com). All constructs were verified by sequencing. HEK293 cells were obtained from the American Type Culture Collection. HEK293 cells were cultured in MEM supplemented with 10% fetal bovine serum (FBS), and 50µg/ml each penicillin and streptomycin at 37°C in a humidified, 5% CO₂ incubator. Cells were transfected with the corresponding cDNAs using Lipofectamine2000 (Life Science) and following manufacturer instructions.

Uptake Assay- HEK293 cells were seeded (1 to 1.5x10⁵ cells per well) in 24-wells plates pre-coated with poly-D-Lysine. The uptake assay was carried out 48h after the transfection. Before the experiment, cells were washed once with uptake buffer containing (in mM): 5 Tris base, 7.5 HEPES, 120 NaCl, 5.4 KCl, 1.2 CaCl₂, 1.2 MgSO₄, 0.1 ascorbic acid, 0.1 pargyline, 1 tropolone and 5 glucose at pH 7.4. The uptake experiment was performed at 37°C. The accumulation of radiolabeled dopamine (3,4-[³H] dihydroxyphenylethylamine, 146.0Ci/mmol; PerkinElmer), started with the addition of labeled (0.02µM) and non-labeled dopamine (10.0µM) in a final volume of 0.4 ml. After 5min, cells were washed with ice-cold NaCl-free uptake buffer (LiCl-based) to stop uptake activity, and lysed with 0.4ml 1% SDS. The incorporated [³H]-DA was measured by liquid scintillation counting with a LSC6000 counter (Beckman Coulter). Non-specific uptake was determined with 0.01mM GBR12935. Uptake data were

analyzed with SigmaPlot 12.5 (Systat Software, Inc). All data are represented as percentage of the mean value with respect to the WT group (mean ± s.e.). Every experimental point had a minimum of six replicates per plate. The statistical analysis was performed with a two-tailed t-student test with an accepted significance level at p<0.05.

Surface Biotinylation – HEK293 were seeded and transfected in a poly-D-Lysine 6-well plate. Forty-eight hours later, transfected cells were washed with PBS and incubated with gentle agitation for 30min at 4°C with 1ml of 1.5mg/ml sulfo-NHS-SS-biotin (Thermo Scientific) prepared in Biotinylation buffer (in mM: 150 NaCl, 2 CaCl₂, 10 triethanolamine, pH 7.8). The reaction was quenched by incubating the cells for an additional 10min with 50mM glycine in PBS. Cells were then washed with PBS and incubated in radioimmune precipitation assay buffer (RIPA) (in mM, 10 Tris, 150 NaCl, 1 EDTA, 0.1% SDS, 1% Triton X-100, and 1% sodium deoxycholate, pH 7.4) at 4°C for 1h. Protein concentration was immediately quantified by BCA protein assay (Thermo-Scientific). Equal amounts of protein were incubated overnight with Neutravidin beads (Thermo-Scientific). Then, beads were washed three times with cold RIPA, and biotinylated membrane proteins were eluted in 50 µl of 2x Laemmli sample buffer (Bio-Rad). Samples were separated by SDS-PAGE (10% TGX minigels, Bio-Rad) and transferred to PVDF membranes using Trans-blot Turbo (Bio-Rad). For western blot analysis the anti-DAT antibody (MAB369, Millipore) and an HRP-conjugated secondary antibody (Jackson Immunoresearch Lab) were used. Densitometry analysis of bands was performed with ImageLab (Bio-Rad) and SigmaPlot 12.5. All data is represented as percentage of the mean value of the WT group (mean ± s.e.). The statistical analysis was performed with a two-tailed t-student test with an accepted significance level at p<0.05.

Oxidative Crosslinking-Experiments were performed 48h after transfection of adhered HEK293 cells in 6-well plates. Cells were washed twice with PBS followed by the addition of 0.1 mM CuSO₄ (Sigma-Aldrich) and 0.4mM o-Phenantroline (Sigma-Aldrich) in PBS. The crosslinking reaction was carried out for 5min at room temperature. The reaction was stopped by removal of the reagent and incubation for 20 min with 10mM N-ethylmaleimide to block free sulfhydryl groups. After quenching, we proceeded to the cell lysis and membrane-solubilization following the protocol detailed in Hastrup *et al* (34). After the extraction, 50µl of sample were mixed with 50µl 4x-Laemmli loading buffer (Bio-Rad) without reducing agent and held at room temperature for 30 min before proceed to the analysis by western blot. Samples were separated by SDS-PAGE (Criterion 7.5% TGX, Bio-Rad) and transferred

to PVDF membranes using Trans-blot Turbo (Bio-Rad). For immunodetection the anti-DAT antibody MAB369 (rat, Millipore) and an HRP-conjugated secondary antibody (Jackson ImmunoResearch Lab) were used. Densitometry analysis of bands was performed with ImageLab (Bio-Rad) and SigmaPlot 12.5 (Systat Software). All data are reported

as percentage of the mean value with respect to the WT group (mean \pm s.e.). The statistical analysis was performed with a two-tailed t-student test an accepted significance level at $p < 0.05$.

Acknowledgements

We gratefully acknowledge several useful discussions with Drs Susan G Amara (SGA) and Delany Torres Salazar, and support from NIH grants 1P30DA035778-01A1 and 5R01-GM099738 to IB and ZIA MH002946-04 to SGA and JG-O, and the computing award from the NSF TeraGrid (TG-MCB130006) and the Anton machine (NIH P41GM103712).

Conflict of interest

The authors declare no conflict of interest.

Author contributions

IB, MHC and JGO designed the project. MHC performed the modeling and simulations. JGO, SW and JDP did the experiments. MHC, JGO and IB analyzed the data and wrote the manuscript.

References

1. Amara, S. G.; Sonders, M. S. (1998) Neurotransmitter transporters as molecular targets for addictive drugs. *Drug Alcohol Depend.* **51** (1-2), 87-96
2. Reith, M. (2002) Neurotransmitter transporters: Structure, Function, and Regulations. Humana, Totowa, NJ,
3. Vaughan, R. A.; Foster, J. D. (2013) Mechanisms of dopamine transporter regulation in normal and disease states. *Trends. Pharmacol. Sci.* **34** (9), 489-496
4. Jardetzky, O. (1966) Simple allosteric model for membrane pumps. *Nature* **211** (5052), 969-970
5. Sitte, H. H.; Freissmuth, M. (2015) Amphetamines, new psychoactive drugs and the monoamine transporter cycle. *Trends. Pharmacol. Sci.* **36** (1), 41-50
6. Sitte, H. H.; Schütz, G. J.; Freissmuth, M. (2015) Cooperativity between individual transporter protomers: new data fuelling old complexes. *J. Neurochem.* **133** (2), 163-166
7. Forrest, L. R. (2013) Structural biology. (Pseudo-)symmetrical transport. *Science* **339** (6118), 399-401
8. Singh, S. K.; Piscitelli, C. L.; Yamashita, A.; Gouaux, E. (2008) A competitive inhibitor traps LeuT in an open-to-out conformation. *Science* **322** (5908), 1655-1661
9. Krishnamurthy, H.; Gouaux, E. (2012) X-ray structures of LeuT in substrate-free outward-open and apo inward-open states. *Nature* **481** (7382), 469-474
10. Yamashita, A.; Singh, S. K.; Kawate, T.; Jin, Y.; Gouaux, E. (2005) Crystal structure of a bacterial homologue of Na⁺/Cl⁻-dependent neurotransmitter transporters. *Nature* **437** (7056), 215-223
11. Stockner, T.; Montgomery, T. R.; Kudlacek, O.; Weissensteiner, R.; Ecker, G. F.; Freissmuth, M.; Sitte, H. H. (2013) Mutational analysis of the high-affinity zinc binding site validates a refined human dopamine transporter homology model. *PLoS Comput. Biol.* **9** (2), e1002909

12. Beuming, T.; Shi, L.; Javitch, J. A.; Weinstein, H. (2006) A comprehensive structure-based alignment of prokaryotic and eukaryotic neurotransmitter/Na⁺ symporters (NSS) aids in the use of the LeuT structure to probe NSS structure and function. *Mol. Pharmacol.* **70** (5), 1630-1642
13. Huang, X.; Zhan, C. G. (2007) How dopamine transporter interacts with dopamine: insights from molecular modeling and simulation. *Biophys. J.* **93** (10), 3627-3639
14. Indarte, M.; Madura, J. D.; Surratt, C. K. (2008) Dopamine transporter comparative molecular modeling and binding site prediction using the LeuT(Aa) leucine transporter as a template. *Proteins* **70** (3), 1033-1046
15. Kniazeff, J.; Shi, L.; Loland, C. J.; Javitch, J. A.; Weinstein, H.; Gether, U. (2008) An intracellular interaction network regulates conformational transitions in the dopamine transporter. *J. Biol. Chem.* **283** (25), 17691-17701
16. Cheng, M. H.; Bahar, I. (2013) Coupled global and local changes direct substrate translocation by neurotransmitter-sodium symporter ortholog LeuT. *Biophys. J.* **105** (3), 630-639
17. Cheng, M. H.; Bahar, I. (2014) Complete mapping of substrate translocation highlights the significance of LeuT N-terminal segment in regulating transport cycle. *PLoS Comput. Biol.* **10** (10), e1003879
18. Khafizov, K.; Perez, C.; Koshy, C.; Quick, M.; Fendler, K.; Ziegler, C.; Forrest, L. R. (2012) Investigation of the sodium-binding sites in the sodium-coupled betaine transporter BetP. *Proc. Natl. Acad. Sci. USA* **109** (44), E3035-3044
19. Shaikh, S. A.; Tajkhorshid, E. (2010) Modeling and dynamics of the inward-facing state of a Na⁺/Cl⁻ dependent neurotransmitter transporter homologue. *PLoS Comput. Biol.* **6** (8), e1000905
20. Thomas, J. R.; Gedeon, P. C.; Grant, B. J.; Madura, J. D. (2012) LeuT conformational sampling utilizing accelerated molecular dynamics and principal component analysis. *Biophys. J.* **103** (1), L1-3
21. Zomot, E.; Bahar, I. (2012) A conformational switch in a partially unwound helix selectively determines the pathway for substrate release from the carnitine/gamma-butyrobetaine antiporter CaiT. *J. Biol. Chem.* **287** (38), 31823-31832
22. Zomot, E.; Gur, M.; Bahar, I. (2015) Microseconds simulations reveal a new sodium-binding site and the mechanism of sodium-coupled substrate uptake by LeuT. *J. Biol. Chem.* **290** (1), 544-555
23. Gur, M.; Zomot, E.; Cheng, M. H.; Bahar, I. (2015) Energy landscape of LeuT from molecular simulations. *J. Chem. Phys.* **143**, 243134
24. Penmatsa, A.; Wang, K. H.; Gouaux, E. (2013) X-ray structure of dopamine transporter elucidates antidepressant mechanism. *Nature* **503** (7474), 85-90
25. Wang, K. H.; Penmatsa, A.; Gouaux, E. (2015) Neurotransmitter and psychostimulant recognition by the dopamine transporter. *Nature* **521** (7552), 322-327
26. Cheng, M. H.; Block, E.; Hu, F.; Cobanoglu, M. C.; Sorkin, A.; Bahar, I. (2015) Insights into the modulation of dopamine transporter function by amphetamine, orphenadrine and cocaine binding. *Front. Neurol.* **6**, 134
27. Cheng, M. H.; Bahar, I. (2015) Molecular Mechanism of Dopamine Transport by Human Dopamine Transporter. *Structure* **23** (11), 2171-2181
28. Khelashvili, G.; Stanley, N.; Sahai, M. A.; Medina, J.; LeVine, M. V.; Shi, L.; De Fabritiis, G.; Weinstein, H. (2015) Spontaneous inward opening of the dopamine transporter is triggered by PIP₂-regulated dynamics of the N-terminus. *ACS Chem. Neurosci.* **6** (11), 1825-1837
29. Hamelberg, D.; de Oliveira, C. A.; McCammon, J. A. (2007) Sampling of slow diffusive conformational transitions with accelerated molecular dynamics. *J. Chem. Phys.* **127** (15), 155102

30. Miao, Y.; Nichols, S. E.; Gasper, P. M.; Metzger, V. T.; McCammon, J. A. (2013) Activation and dynamic network of the M2 muscarinic receptor. *Proc. Natl. Acad. Sci. USA* **110** (27), 10982-10987
31. Coleman, J. A.; Green, E. M.; Gouaux, E. (2016) X-ray structures and mechanism of the human serotonin transporter. *Nature* **532** (7599), 334-339
32. Wang, H.; Elferich, J.; Gouaux, E. (2012) Structures of LeuT in bicelles define conformation and substrate binding in a membrane-like context. *Nat. Struct. Mol. Biol.* **19** (2), 212-219
33. Berger, S. P.; Farrell, K.; Conant, D.; Kempner, E. S.; Paul, S. M. (1994) Radiation inactivation studies of the dopamine reuptake transporter protein. *Mol. Pharmacol.* **46** (4), 726-731
34. Hastrup, H.; Karlin, A.; Javitch, J. A. (2001) Symmetrical dimer of the human dopamine transporter revealed by cross-linking Cys-306 at the extracellular end of the sixth transmembrane segment. *Proc. Natl. Acad. Sci. USA* **98** (18), 10055-10060
35. Torres, G. E.; Carneiro, A.; Seamans, K.; Fiorentini, C.; Sweeney, A.; Yao, W. D.; Caron, M. G. (2003) Oligomerization and trafficking of the human dopamine transporter. Mutational analysis identifies critical domains important for the functional expression of the transporter. *J. Biol. Chem.* **278** (4), 2731-2739
36. Kilic, F.; Rudnick, G. (2000) Oligomerization of serotonin transporter and its functional consequences. *Proc. Natl. Acad. Sci. USA* **97** (7), 3106-3111
37. Sorkina, T.; Doolen, S.; Galperin, E.; Zahniser, N. R.; Sorkin, A. (2003) Oligomerization of dopamine transporters visualized in living cells by fluorescence resonance energy transfer microscopy. *J. Biol. Chem.* **278** (30), 28274-28283
38. Anderluh, A.; Klotzsch, E.; Reismann, A. W. A. F.; Brameshuber, M.; Kudlacek, O.; Newman, A. H.; Sitte, H. H.; Schütz, G. J. (2014) Single molecule analysis reveals coexistence of stable serotonin transporter monomers and oligomers in the live cell plasma membrane. *J. Biol. Chem.* **289**, 4387-94
39. Schmid, J. A.; Scholze, P.; Kudlacek, O.; Freissmuth, M.; Singer, E. A.; Sitte, H. H. (2001) Oligomerization of the human serotonin transporter and of the rat GABA transporter 1 visualized by fluorescence resonance energy transfer microscopy in living cells. *J. Biol. Chem.* **276** (6), 3805-3810
40. Scholze, P.; Freissmuth, M.; Sitte, H. H. (2002) Mutations within an intramembrane leucine heptad repeat disrupt oligomer formation of the rat GABA transporter 1. *J. Biol. Chem.* **277** (46), 43682-43690
41. Sitte, H. H.; Farhan, H.; Javitch, J. A. (2004) Sodium-dependent neurotransmitter transporters: oligomerization as a determinant of transporter function and trafficking. *Mol. Interv.* **4** (1), 38-47
42. Zhen, J.; Antonio, T.; Cheng, S. Y.; Ali, S.; Jones, K. T.; Reith, M. E. A. (2015) Dopamine transporter oligomerization: impact of combining protomers with differential cocaine analog binding affinities. *J. Neurochem.* **133** (2), 167-173
43. Seidel, S.; Singer, E. A.; Just, H.; Farhan, H.; Scholze, P.; Kudlacek, O.; Holy, M.; Koppatz, K.; Krivanek, P.; Freissmuth, M. (2005) Amphetamines take two to tango: an oligomer-based counter-transport model of neurotransmitter transport explores the amphetamine action. *Mol. Pharmacol.* **67** (1), 140-151
44. Sitte, H. H.; Freissmuth, M. (2010) The reverse operation of Na⁺/Cl⁻-coupled neurotransmitter transporters - why amphetamines take two to tango. *J. Neurochem.* **112** (2), 340-355
45. Comeau, S. R.; Gatchell, D. W.; Vajda, S.; Camacho, C. J. (2004) ClusPro: an automated docking and discrimination method for the prediction of protein complexes. *Bioinformatics* **20** (1), 45-50

46. Bartholomäus, I.; Milan-Lobo, L.; Nicke, A.; Dutertre, S.; Hastrup, H.; Jha, A.; Gether, U.; Sitte, H. H.; Betz, H.; Eulenburg, V. (2008) Glycine transporter dimers: Evidence for occurrence in the plasma membrane. *J. Biol. Chem.* **283** (16), 10978-10991
47. Chen, N.; Reith, M. E. A. (2008) Substrates dissociate dopamine transporter oligomers. *J. Neurochem.* **105** (3), 910-920
48. Gur, M.; Cheng, M. H.; Zomot, E.; Bahar, I. (2017) Effect of dimerization on the dynamics of neurotransmitter: sodium symporters. *J. Phys. Chem. B*, **121** (15), 3657–3666.
49. Atilgan, A. R.; Durell, S. R.; Jernigan, R. L.; Demirel, M. C.; Keskin, O.; Bahar, I. (2001) Anisotropy of fluctuation dynamics of proteins with an elastic network model. *Biophys. J.* **80** (1), 505-515.
50. Jiang, J.; Shrivastava, I. H.; Watts, S. D.; Bahar, I.; Amara, S. G. (2011) Large collective motions regulate the functional properties of glutamate transporter trimers. *Proc. Natl. Acad. Sci. U. S. A* **108** (37), 15141-15146
51. Verdon, G.; Boudker, O. (2012) Crystal structure of an asymmetric trimer of a bacterial glutamate transporter homolog. *Nat. Struct. Mol. Biol.* **19** (3), 355-357
52. Koshy, C.; Schweikhard, E. S.; Gärtner, R. M.; Perez, C.; Yildiz, +.; Ziegler, C. (2013) Structural evidence for functional lipid interactions in the betaine transporter BetP. *EMBO. J.* **32** (23), 3096-3105
53. Anderluh, A.; Hofmaier, T.; Klotzsch, E.; Kudlacek, O.; Stockner, T.; Sitte, H. H.; Schütz, G. J. (2017) Direct PIP₂ binding mediates stable oligomer formation of the serotonin transporter. *Nat. Commun.* **8**, 14089
54. Shaw, D. E.; Deneroff, M. M.; Dror, R. O.; Kuskin, J. S.; Larson, R. H.; Salmon, J. K.; Young, C.; Batson, B.; Bowers, K. J.; Jack C. Chao; Eastwood, M. P.; Gagliardo, J.; Grossman, J. P.; Ho, C. R.; Ierardi, D. J.; Kolossváry, I.; Klepeis, J. L.; Layman, T.; McLeavey, C.; Moraes, M. A.; Mueller, R.; Priest, E. C.; Shan, Y.; Spengler, J.; Theobald, M.; Towles, B.; Wang, S. C. (2008) Anton, A Special-Purpose Machine for Molecular Dynamics Simulation. *Commun ACM* **51** (7), 91-97
55. Humphrey, W.; Dalke, A.; Schulten, K. (1996) VMD: visual molecular dynamics. *J. Mol. Graph.* **14** (1), 33-38
56. Phillips, J. C.; Braun, R.; Wang, W.; Gumbart, J.; Tajkhorshid, E.; Villa, E.; Chipot, C.; Skeel, R. D.; Kale, L.; Schulten, K. (2005) Scalable molecular dynamics with NAMD. *J. Comput. Chem.* **26** (16), 1781-1802
57. Klauda, J. B.; Venable, R. M.; Freites, J. A.; O'Connor, J. W.; Tobias, D. J.; Mondragon-Ramirez, C.; Vorobyov, I.; MacKerell, A. D., Jr.; Pastor, R. W. (2010) Update of the CHARMM all-atom additive force field for lipids: validation on six lipid types. *J. Phys. Chem. B* **114**, 7830-7843
58. Mackerell, A. D., Jr.; Feig, M.; Brooks, C. L. 3. (2004) Extending the treatment of backbone energetics in protein force fields: limitations of gas-phase quantum mechanics in reproducing protein conformational distributions in molecular dynamics simulations. *J. Comput. Chem.* **25** (11), 1400-1415
59. Vanommeslaeghe, K.; Hatcher, E.; Acharya, C.; Kundu, S.; Zhong, S.; Shim, J.; Darian, E.; Guvench, O.; Lopes, P.; Vorobyov, I.; Mackerell, A. D., Jr. (2010) CHARMM general force field: A force field for drug-like molecules compatible with the CHARMM all-atom additive biological force fields. *J. Comput. Chem.* **31** (4), 671-690

Footnotes

[†]These authors contributed equally to this work.

^{*}This work was supported by the National Institutes of Health Grants 5R01-GM099738, 1P30DA035778-01A1, and P41GM103712-01 to IB, and MH002946 to SGA and JG-O

[#]To whom correspondence should be addressed: Dept. of Computational and Systems Biology, School of Medicine, University of Pittsburgh, 3064 BST 3, 3501 Fifth Avenue, Pittsburgh, PA 15213. Tel: 412 648 3332 ; Fax: 412 648 3163; bahar@pitt.edu

²The abbreviations used are: NSS, neurotransmitter:sodium symporter; DA, dopamine; DAT, dopamine transporter; hDAT, human dopamine transporter; EC, extracellular; IC, intracellular; TM, transmembrane; OF_o, outward-facing open; OF_c, outward-facing closed; IF_o, inward-facing open; SERT, serotonin transporter; MD, molecular dynamics; BetP, betamine transporter; LeuT, leucine transporter; CoM, center-of-mass; RMSD, root-mean-squared deviation, 1-palmitoyl-2-oleoyl-sn-glycero-3-phosphocholine (POPC); PG, palmitoyl-oleoyl phosphatidyl glycerol; NET, norepinephrine transporter; GAT1, GABA transporter 1. GLY1, glycine transporter 1.

Figures and figure legends

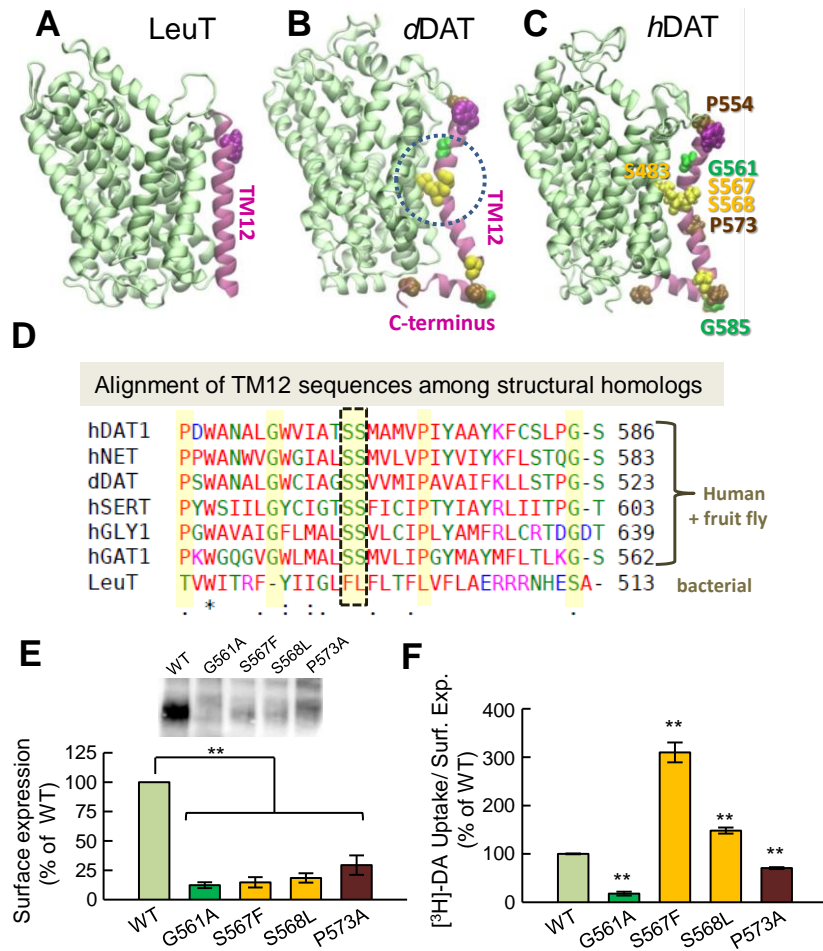


Figure 1: The kink in the TM12 segment of DAT and its functional significance. Structural and sequence differences between (A) LeuT from *Aquifex aeolicus*, (B) dDAT from *Drosophila melanogaster*, and (C) hDAT (human). There is a kink (dashed circle in B) in the TM12 segment of eukaryotic DATs near two serines conserved among the eukaryotic transporters. DAT has an additional C-terminal helix, with a glycine (G585 in hDAT) conserved among human paralogs. Notably, S568 forms hydrogen bonding with S483 in the TM10 segment. (D) Sequence alignment of TM12 in different members of transporters that share the LeuT fold. The sequences belong to human paralogs hDAT, hNET, hSERT, hGLY1, and hGAT1, and the fruit fly DAT, dDAT, shown in B. The last sequence is that of bacterial LeuT (shown in A). Selected residues conserved among all human paralogs are highlighted in yellow (also labeled in panel C). The kink-forming serines on TM12 are highlighted and enclosed in a dashed box. (E-F) Effect of mutations at TM12 kink-forming residues on DAT expression and DA uptake. (E) Surface expression of WT, G561A, S567F, S568L and P573A hDAT. Transfected HEK293 cells were incubated with sulfo-NHS-SS-biotin and isolated with neutravidin-agarose beads after cell lysis. For detection of DAT protein an anti-DAT (rat, Millipore MAB369) antibody was used. Densitometry analysis was performed with ImageLab (Bio-Rad) and SigmaPlot 12.5 (Systat Software). Bars represent the percentage of the mean value of the WT group (mean \pm s.e.). (F) Transport activity. Uptake of [3 H]-DA was performed in HEK293 cells. DA-accumulation was normalized with respect to the percentage of cell surface expression for each mutant, and expressed as percentage of WT. The statistical analysis was performed with a two-tailed t-student test versus WT group with an accepted significance level of ** $p < 0.05$.

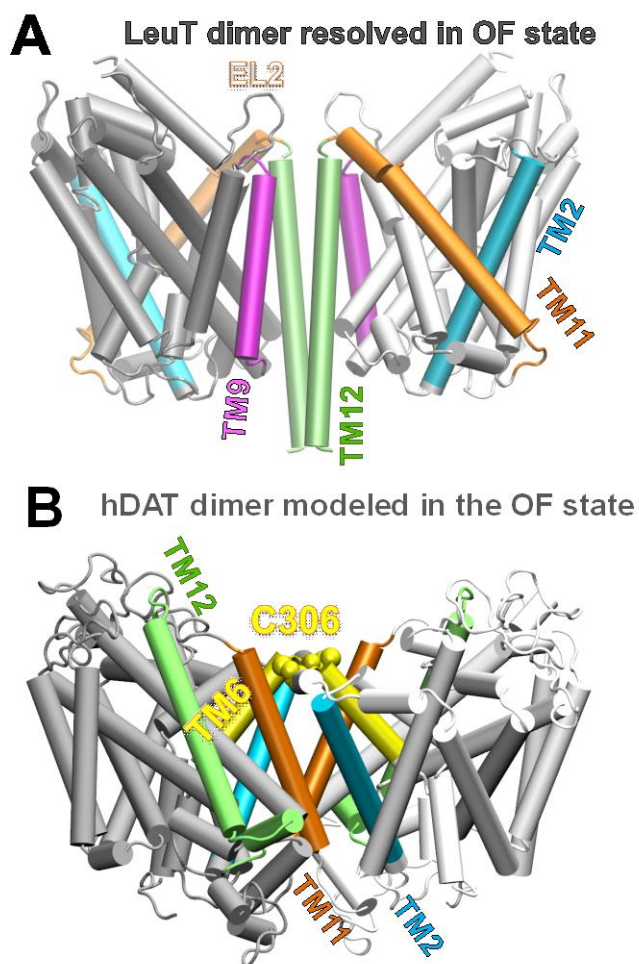


Figure 2: Difference in dimerization architecture between the known LeuT dimer and the computationally-predicted hDAT dimer in the outward-facing conformation. (A) LeuT dimer has interfacial TM segments TM9 (*purple*) and TM12 (*lime*); and (B) computationally-predicted hDAT dimer makes interfacial contacts between TM6 (*yellow*), TM11 (*orange*) and TM2 (*cyan*) helices.

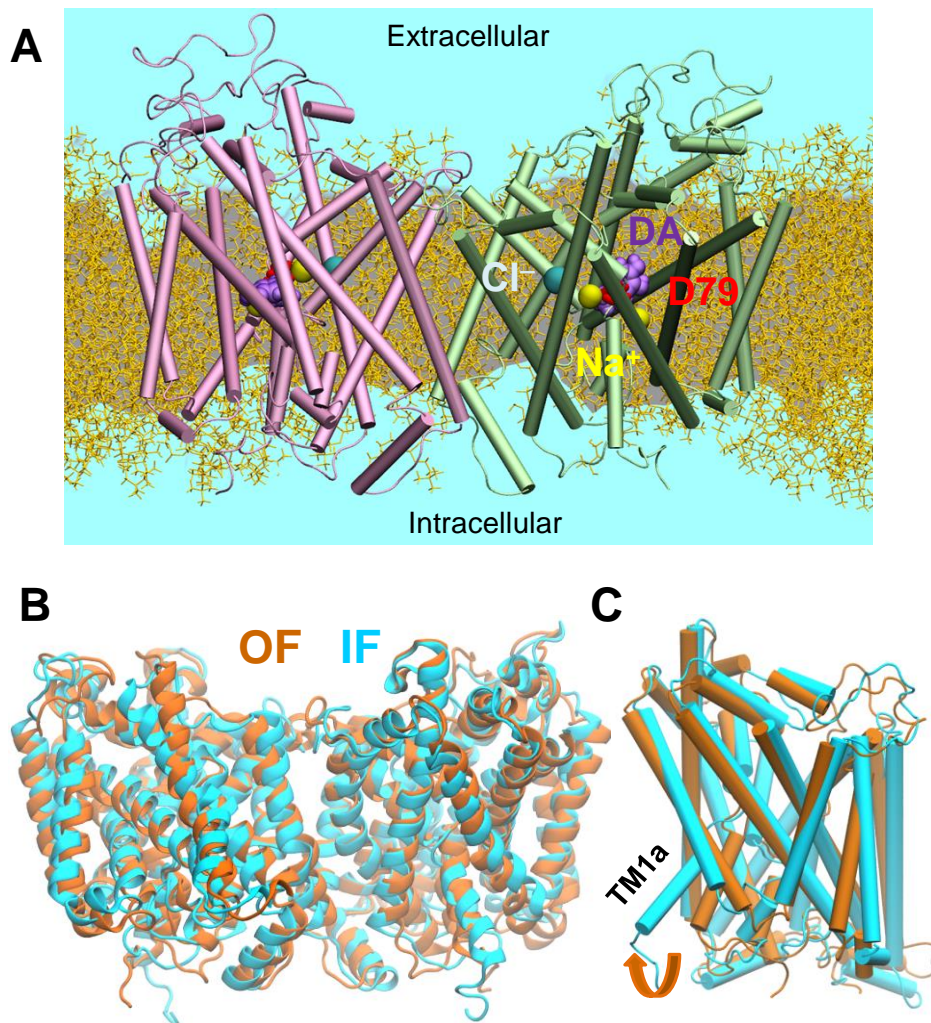


Figure 3: MD simulations of hDAT dimer dynamics, embedded into membrane lipids. (A) Typical MD set up for *hDAT* dimer (colored in *pink* and *green*) in a lipid bilayer (*yellow licorice* format) and solvated by 0.15 M NaCl (not shown; *light blue*). The bound substrate DA, and the co-transported Na⁺ and Cl⁻ are represented by *purple, yellow* and *cyan spheres*. (B) Alignment of 100-ns MD equilibrated *hDAT* dimer in the outward-facing (OF; *orange ribbon diagram*) and inward-facing (IF; *cyan*) state. The RMSD between the OF and IF dimers levels off at 3.4 ± 0.3 Å; and (C) Comparison of helical orientations in the OF and IF states. For clarity, one monomer (in *cartoon* format) taken from the dimer is shown for each state.

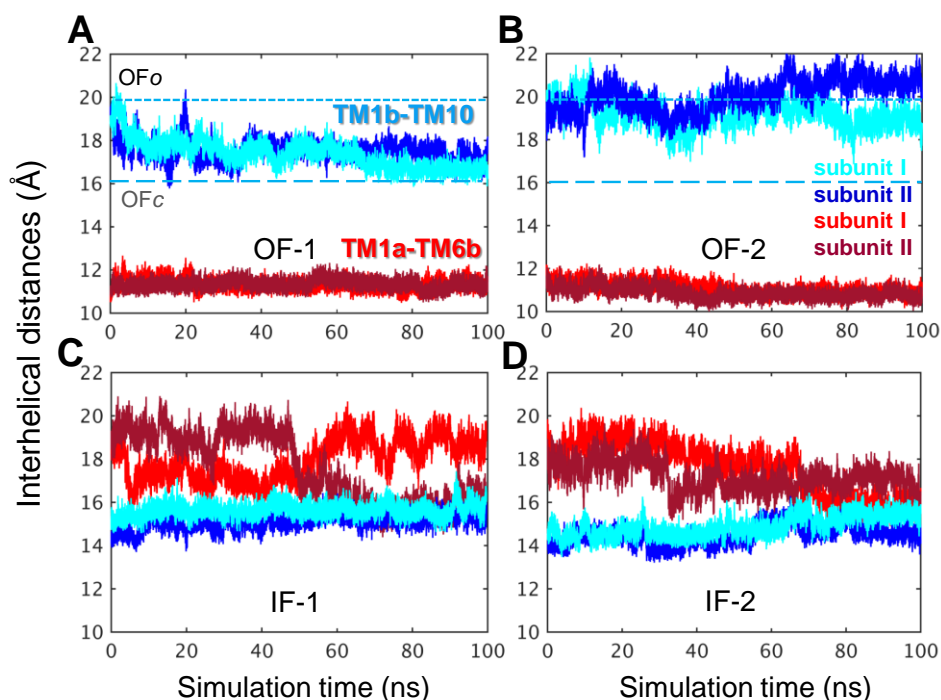


Figure 4: Time-evolution of the interhelical distances. The opening/closure of the EC and IC vestibules is characterized by the respective interhelical distances of the EC-exposed TM1b-TM10 and the IC-exposed TM1a-TM6b, shown for both subunits, as labeled (see refs (26,27)). Results from four runs are presented: **(A)** OF_1, in which the closure of the EC vestibule led to the outward-facing *closed* (OFC) state in both subunits; **(B)** OF_2, in which both subunits remained in the outward-facing *open* (OFO) state; as indicated by the separation between the EC-exposed TM1b and TM10 segments (*light and dark blue*), and the close proximity of the of the IC-exposed helical segments TM1a-TM6b (*light and dark red*); **(C)** IF_1, in which the IC vestibule remained open in both subunits (see the *red curves*); and **(D)** IF_2, in which the initiation of a transition to the OF conformation could be observed but the IC vestibule remained open in both subunits. The characteristic distances for TM1b-TM10 obtained in the hDAT dimer simulations are 20.0 ± 2.0 Å and 16.5 ± 0.5 Å in the OFO and OFC states, respectively. These values closely approximate those reported for hDAT monomer simulations (27). Distances are indicated by *dotted* and *dashed* lines in panels **A** and **B**. In the OF state, the distance between the IC-exposed segments TM1a and TM6b remained 11.5 ± 1.0 Å, same as that reported in the monomer simulations (27). In the inward-facing *open* (IFO) state, the IC vestibule is open for DA release when the distance between TM1a and TM6b is greater than 15 Å in hDAT monomer (see ref. (27)).

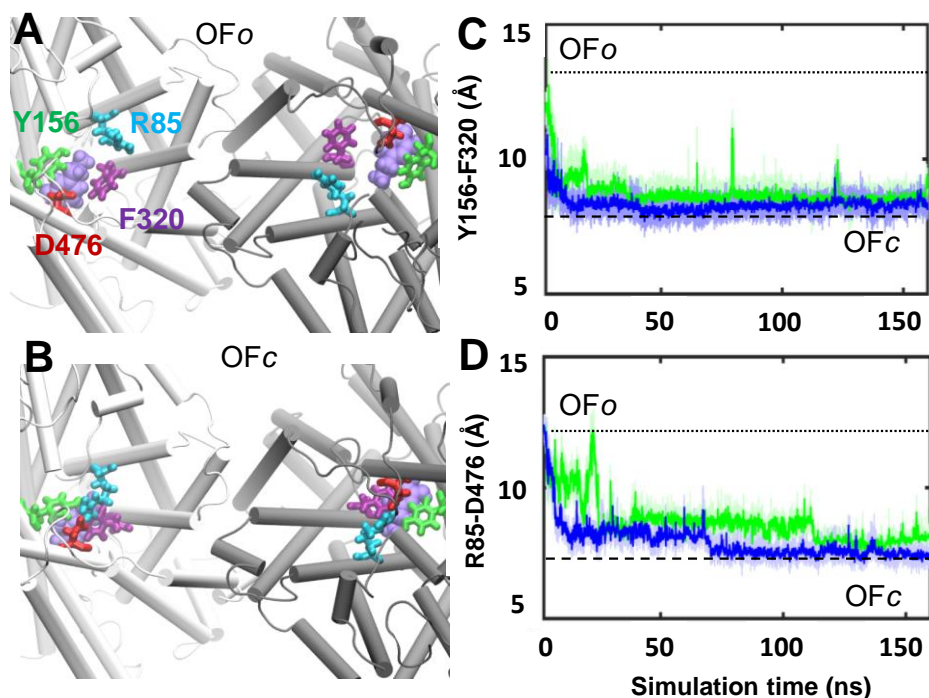


Figure 5: Structural transition observed from the OFo to OFc in the hDAT dimer. Top view of (A) the initial OFo state with the opening of two EC gates: R85-D476 and Y156-F320; and (B) closure of the EC gates in the OFc state; snapshot around 160 ns was used. Time evolution of the center of the mass distances between the two EC gating residue pairs (C) aromatic residues Y156 and F320; and (D) salt-bridge forming residue pairs R85 and D476. Note that the closure of the gates occurred almost simultaneously in the two subunits (colored in *green* and *blue*).

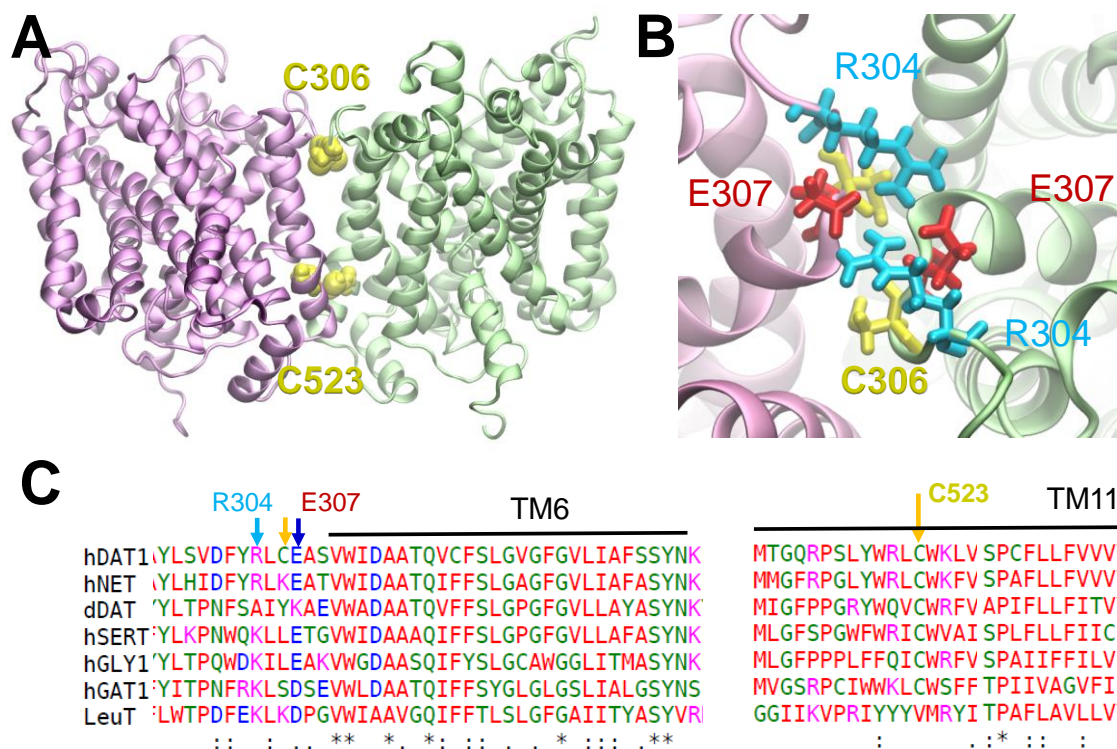


Figure 6: Interfacial interactions. (A) Two interfacial cysteines between subunits I and II (colored *pink* and *green*) are likely to form cross-links between the dimers: C306(I) – C306(II) (superposed, not seen separately in the panel) and C523(I) – C523(II). They are within close distance (< 11 Å) in both the OF and IF conformers. (B) An interfacial salt bridge is likely to form between E307 and R304 in the IF conformation of the dimer. (C) Sequence alignment of the putative interfacial regions.

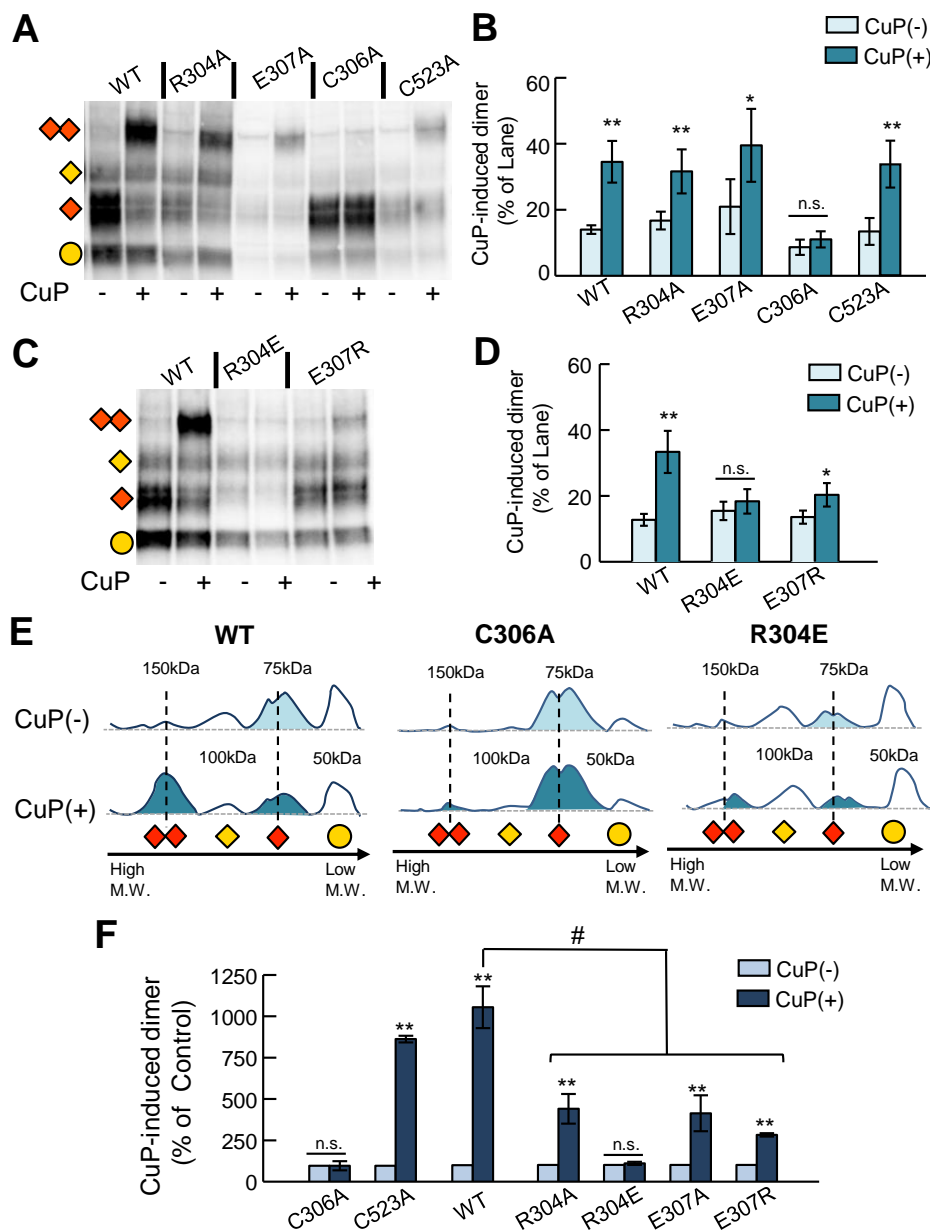


Figure 7: Oxidative cross-linking of DAT C306 in TM6 hDAT mutants. (A) Representative blot of CuP crosslinking in intact cells WT and DAT mutants R304A, E307A, C306A and C523A. Cross-linking reaction with 0.1 μ M CuSO₄ and 0.4 μ M Phenantroline was performed for 5 minutes at room temperature. Detection of DAT protein was detected by western blot using an anti-DAT (rat, Millipore MAB369) antibody. Different immunodetected DAT bands were detected in CuP non-treated(-) and treated lanes (+). Different transporter forms are indicated as follows: immature monomer (yellow circle), mature monomer (red rombus), immature dimer (yellow rombus), mature dimer (double red rombus). (B) Quantification of the CuP-induced 150kDa-DAT abduct. Bars represent the intensity of the band as % of the total bands per lane. Densitometry analysis was performed with ImageLab (Bio-Rad) and SigmaPlot 12.5 (Systat Software). (C-D) CuP crosslinking of WT, R304E and E307R. (E) The intensity lane profile (obtained with Imagelab software) shows the relative position of the different DAT-forms for WT, C306A and R304E. The shadowed peaks represent the mature forms (monomeric-75kDa) and CuP-induced dimer (150kDa). (F) Quantification of the CuP-induced dimers relative to the 150kDa-DAT band in the control group (CuP(-)) for each DAT construct. Bars represent the mean values (mean \pm s.e.). *p < 0.05 and ** p < 0.01 for Student t-test p value versus control group. # Represents p < 0.05 Anova one-way.

Table 1. Effects of hDAT mutations on transport activity and cell surface expression

Construct	[³ H]-DA Uptake (% of WT)	Surface Expression (% of WT)	[³ H]-DA uptake/Surface Expression
WT-hDAT	100.0 ± 0.8 (n=8)	100	100
G561A	2.2 ± 0.5 (n=6)	12.3 ± 2.5 (n=3)	17.9 ± 4.1**
S567F	45.6 ± 3.0 (n=6)	14.7 ± 4.4 (n=3)	309.7 ± 20.6**
S568L	27.4 ± 1.2 (n=10)	18.5 ± 4.0 (n=3)	148.2 ± 6.3**
P573A	20.8 ± 0.6 (n=6)	29.4 ± 8.2 (n=3)	70.7 ± 2.0**
C306A	122.8 ± 1.9 (n=6)	127.2 ± 15.1 (n=4)	96.5 ± 1.5 ^{n.s.}
C523A	90.4 ± 2.5 (n=10)	49.3 ± 5.6 (n=6)	183.3 ± 5.2*
R304A	80.1 ± 1.9 (n=6)	22.3 ± 1.5 (n=4)	359.3 ± 8.3**
E307A	82.7 ± 1.6 (n=6)	31.1 ± 4.3 (n=4)	265.5 ± 5.0**
R304E	31.2 ± 1.3 (n=6)	10.0 ± 2.8 (n=6)	313.7 ± 12.7**
E307R	70.1 ± 1.3 (n=6)	44.2 ± 9.2 (n=5)	158.6 ± 2.9*

Transport activity and cell surface biotinylation experiments were performed in HEK293 cells transfected with hDAT WT and mutants (See Experimental Procedure). Values for uptake and surface expression are expressed as mean ± s.e. and calculated as percentage of the mean value for the WT group in every independent experiment (n). Statistical values were obtained with Student t-test with significance values of **p < 0.001 and *p < 0.05.

**Allosteric Modulation of Human Dopamine Transporter Activity under Conditions
Promoting its Dimerization**

Mary Hongying Cheng, Jennie Garcia-Olivares, Steven Wasserman, Jennifer DiPietro and
Ivet Bahar

J. Biol. Chem. published online June 5, 2017

Access the most updated version of this article at doi: [10.1074/jbc.M116.763565](https://doi.org/10.1074/jbc.M116.763565)

Alerts:

- [When this article is cited](#)
- [When a correction for this article is posted](#)

[Click here](#) to choose from all of JBC's e-mail alerts

Supplemental material:

<http://www.jbc.org/content/suppl/2017/06/05/M116.763565.DC1>

This article cites 0 references, 0 of which can be accessed free at

<http://www.jbc.org/content/early/2017/06/05/jbc.M116.763565.full.html#ref-list-1>